# Growth, structure, and polarized spectroscopy of monoclinic Er 3+ :MgWO 4 crystal

Lizhen Zhang, Liza Basyrova, Pavel Loiko, Patrice Camy, Zhoubin Lin, Ge Zhang, Sami Slimi, Rosa Maria Solé, Xavier Mateos, Magdalena Aguiló, et al.

*To be published in Optical Materials Express:*

**Title:** Growth, structure and polarized spectroscopy of monoclinic $Er^{3+}$:MgWO crystal

**Authors:** Weidong Chen,lizhen zhang,liza Basyrova,Pavel Loiko,Patrice Camy,zhoubin lin,Zhang Ge,Sami Slimi,Xavier Mateos,Magdalena Aguilo,Francesc Diaz,Elena Dunina,Alexei Kornienko,Li Wang,Valentin Petrov,Uwe Griebner,Rosa Maria Solé

**Accepted:** 12 April 22

**Posted** 13 April 22

**DOI:** https://doi.org/10.1364/OME.449649

# Growth, structure and polarized spectroscopy of monoclinic $Er^{3+}$:$MgWO_4$ crystal


**Lizhen Zhang,[1] Liza Basyrova,[2] Pavel Loiko,[2] Patrice Camy,[2] Zhoubin Lin,[1] Ge Zhang,[1] Sami Slimi,[3] Rosa Maria Solé,[3] Xavier Mateos,[3] Magdalena Aguiló,[3] Francesc Díaz,[3] Elena Dunina,[4] Alexey Kornienko,[4] Uwe Griebner,[5] Valentin Petrov,[5] Li Wang,[5] and Weidong Chen[1,5,*]**

[1]*Fujian Institute of Research on the Structure of Matter, Chinese Academy of Sciences, 350002 Fuzhou, China*
[2]*Centre de Recherche sur les Ions, les Matériaux et la Photonique (CIMAP), UMR 6252 CEA-CNRS-ENSICAEN, Université de Caen, 6 Boulevard Maréchal Juin, 14050 Caen Cedex 4, France*
[3]*Universitat Rovira i Virgili, Física i Cristal·lografia de Materials i Nanomaterials (FiCMA-FiCNA)-Marcel·lí Domingo 1, 43007 Tarragona, Spain*
[4]*Vitebsk State Technological University, 72 Moskovskaya Ave., 210035 Vitebsk, Belarus*
[5]*Max Born Institute for Nonlinear Optics and Short Pulse Spectroscopy, Max-Born-Str. 2a, 12489 Berlin, Germany*
**chenweidong@fjirsm.ac.cn*



**Abstract:** We report on the growth, structure and polarized spectroscopy of a novel promising laser crystal, erbium-doped magnesium monotungstate, $Er^{3+}$:$MgWO_4$. 1.01 t.% $Er^{3+}$:$MgWO_4$ was grown by the Top-Seeded Solution Growth method using $Na_2WO_4$ as a solvent. The crystal structure was refined by the Rietveld method. $Er^{3+}$:$MgWO_4$ belongs to the monoclinic class (sp. gr. *P*2/*c*, wolframite-type structure, lattice parameters: $a$ = 4.6939(6) Å, $b$ = 5.6747(4) Å, $c$ = 4.9316(6) Å and $\beta$ = 90.7858(4) Å. The transition intensities for $Er^{3+}$ ions were determined using the Judd-Ofelt theory accounting for an intermediate configuration interaction (ICI). $Er^{3+}$ ions in $MgWO_4$ exhibit intense, strongly polarized and broad absorption and emission bands owing to their accommodation in distorted low-symmetry sites ($C_2$). The stimulated-emission cross-section for the $^4I_{13/2} \rightarrow {}^4I_{15/2}$ transition is $0.31\times10^{-20}$ cm$^2$ at 1637 nm (light polarization: $\boldsymbol{E} \parallel \boldsymbol{b}$). The radiative lifetime of the $^4I_{13/2}$ state is 4.85 ± 0.05 ms. The multiphonon non-radiative relaxation for $Er^{3+}$ excited multiplets is quantified. $Er^{3+}$ ions in $MgWO_4$ feature large Stark splitting of the ground-state, $\Delta E(^4I_{15/2})$ = 435 cm$^{-1}$. $Er^{3+}$:$MgWO_4$ is attractive for low-threshold lasers at ~1.64 μm.




## 1. Introduction

The Erbium ion ($Er^{3+}$) is well known for its emission in the eye-safe spectral range of ~1.5 - 1.6 μm originating from the $^4I_{13/2} \rightarrow {}^4I_{15/2}$ electronic transition. The applications of eye-safe erbium lasers are in the fields of range-finding, environmental sensing, aerial navigation and telecom. So far, $Er^{3+}$,$Yb^{3+}$-codoped phosphate glasses represent the state-of-the-art erbium laser media [1]. Here, the $Yb^{3+}$ ion acts as a sensitizer to enhance the pump absorption at ~0.96 - 0.98 μm, the spectral range addressed by commercial InGaAs laser diodes [2]. Such glasses feature attractive spectroscopic behavior, i.e., broadband $Yb^{3+}$ absorption, efficient $Yb^{3+} \rightarrow Er^{3+}$ energy transfer and long $Er^{3+}$ upper laser lifetime. Er,Yb:phosphate glass lasers can generate mJ-level nanosecond pulses making them ideal for portable range-finders [3]. At the same time, glasses suffer from poor thermo-mechanical properties limiting the power scaling capabilities.

As an alternative to glassy gain media, single crystals can be used. However, so far, only a few materials were found to be suitable for efficient lasers based on the $Yb^{3+}$,$Er^{3+}$ codoping scheme. These include vanadates ($YVO_4$ [4]), borates ($REAl_3(BO_3)_4$ [5,6], $RECa_4O(BO_3)_3$ [7]), and silicates ($Y_2SiO_5$ [8]). Tolstik *et al.* demonstrated an Er,Yb:$YAl_3(BO_3)_4$ (Er,Yb:YAB) laser delivering an output power of 1 W at 1555 nm with a slope efficiency of 35% [5]. Still, further power scaling of such lasers is limited by severe thermo-optic effects originating from upconversion losses. Moreover, the growth technology of $REAl_3(BO_3)_4$ borate crystals is far from being mature.

An alternative approach is the use of singly $Er^{3+}$-doped crystals which can be pumped at ~1.54 μm. This corresponds to excitation directly to the upper laser level (in-band or resonant pumping). Owing to the relatively high absorption cross-sections for the $^4I_{15/2} \rightarrow {}^4I_{13/2}$ $Er^{3+}$ transition, high pump efficiencies can be achieved even for low $Er^{3+}$ doping levels (~1 at.%). This leads to weak energy-transfer upconversion, which, together with the low quantum effect inherent to the resonant pumping scheme, determines weak heat loading and high laser slope efficiencies. Contrary to the $Er^{3+}$, $Yb^{3+}$ codoping scheme for which only a few particular host matrices are suitable, single $Er^{3+}$ doping is more advantageous from the material point of view: efficient laser operation can be achieved in many singly $Er^{3+}$-doped laser materials (crystals) under in-band pumping. In-band pumped Er:$Y_3Al_5O_{12}$ (Er:YAG) lasers have delivered multi-watt output at 1617 nm and 1645 nm [9,10]. However, one disadvantage of cubic Er:YAG crystals are the depolarization losses appearing at high pump powers in lasers containing polarization-selective elements. Thus, it is still important to search for novel singly $Er^{3+}$-doped materials offering intrinsic optical anisotropy, broad and intense spectral bands for polarized light, and good thermo-mechanical properties.

Magnesium monotungstate ($MgWO_4$) has recently emerged as a promising host crystal for doping with laser-active rare-earth ions [11-13]. This crystal is monoclinic and optically biaxial offering strong optical anisotropy. It was found to exhibit good thermo-mechanical properties, i.e., high thermal conductivity of ~8.7 $Wm^{-1}K^{-1}$ [14] and low anisotropy of thermal expansion [13]. High-power laser operation was demonstrated using such crystals: Loiko *et al.* developed a diode-pumped $Yb^{3+}$:$MgWO_4$ laser delivering 18.2 W at ~1056 nm with a high slope efficiency of ~89% and a linearly polarized output [12]. The low-symmetry distorted coordination of rare-earth ions in $MgWO_4$ leads to broad emission bands [15]. Because of the broadband emission properties, such crystals have been implemented in femtosecond mode-locked lasers [16,17]. Although $Er^{3+}$:$MgWO_4$ has never been studied so far, other monoclinic crystals doped with $Er^{3+}$ ions appear promising for the development of eye-safe lasers: Serres *et al.* reported on a diode-pumped 1 at.% Er:$KLu(WO_4)_2$ laser generating 268 mW at 1610 nm with a slope efficiency of 30% [18].

In the present work, we report on the growth, structure refinement and a polarization-resolved spectroscopic study of an $Er^{3+}$-doped $MgWO_4$ crystal, for the first time, to the best of our knowledge.

## 2. Crystal growth and structure

### *2.1 Crystal growth*

$Er^{3+}$:$MgWO_4$ was grown by the top-seeded solution growth (TSSG) method [11,19] from the flux with a composition of $MgWO_4$: $Na_2WO_4$ = 5:7 mol (sodium tungstate, $Na_2WO_4$, was used as a solvent) in a vertical tubular furnace. The starting materials were $Na_2CO_3$, MgO, $WO_3$ (purity: analytical grade) and $Er_2O_3$ (dopant, purity: 99.99%). They were weighed according to the above-mentioned composition with the initial $Er^{3+}$ concentration of 10 at.% (with respect to $Ca^{2+}$). The weighed materials were mixed, ground and then put into a Pt crucible with dimensions of Ø55 × 60 $mm^3$. The crucible was placed into a resistive furnace equipped with a programmable temperature controller, nickel-chrome heating wires and a Pt–Rh/Pt thermocouple. A [010]-oriented seed from an undoped $MgWO_4$ crystal was used. The solution was kept at 980°C for 2 days to ensure that the starting materials melted completely

and homogeneously. The saturation temperature was determined to be 953°C by repeated seeding trials. The crystal was grown at a cooling rate of 0.6 - 1°C/day and a rotation speed of 10 rpm in the temperature range of 953 - 930°C. Once the growth was completed, the crystal was slowly pulled out of the solution and cooled down to room temperature (RT, 293 K) at a rate of 10 K/h. Figure 1 shows an as-grown $Er^{3+}$:$MgWO_4$ crystal with dimensions of 20 × 8 × 6 $mm^3$. It has a rose coloration due to erbium doping.

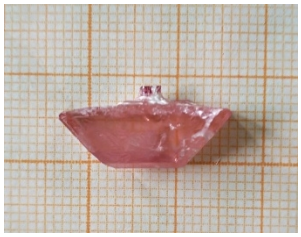

**Fig. 1.** A photograph of the as-grown 1.01 at.% $Er^{3+}$:$MgWO_4$ crystal, the growth direction is along the [010] axis.

The actual $Er^{3+}$ doping level was determined by inductively coupled plasma atomic emission spectrometry (ICP-AES, Ultima2, Jobin-Yvon) to be 1.01 at.% (ion density: $N_{Er}$ = 1.419 × $10^{20}$ at/$cm^3$). No significant variation of the $Er^{3+}$ doping level across the crystal boule was observed. The segregation coefficient of $Er^{3+}$ $K_{Er}$ was then 0.1. Such a low value is due to a significant difference of ionic radii of $Mg^{2+}$ and $Er^{3+}$ (see below). Despite the low $K_{Er}$ value for $MgWO_4$, it is relatively easy to access the desired doping level typical for singly $Er^{3+}$-doped crystals (~1 at.%). Higher doping levels can be accessed by increasing the initial content of $Er^{3+}$ ions in the growth charge or probably by using other charge compensators (e.g., $Li^+$ cations). However, in in-band-pumped Er lasers, the doping levels above 1 at.% are usually not used due to the enhanced energy-transfer upconversion.

### *2.2 Structure refinement and electronic structure*

The X-ray powder diffraction (XRD) data were collected using a Rigaku MiniFlex 600 X-ray diffractometer with CuKα radiation ($\lambda$ = 1.5418 Å) in an angular range of 2θ = 10-80° with a scan step of 0.02° and a scan speed of 5°/min, as shown in Fig. 2(a). The measured XRD pattern was well assigned using a standard diffraction pattern of undoped $MgWO_4$ (JCPDS card #96-101-0643) and no other phases were found.

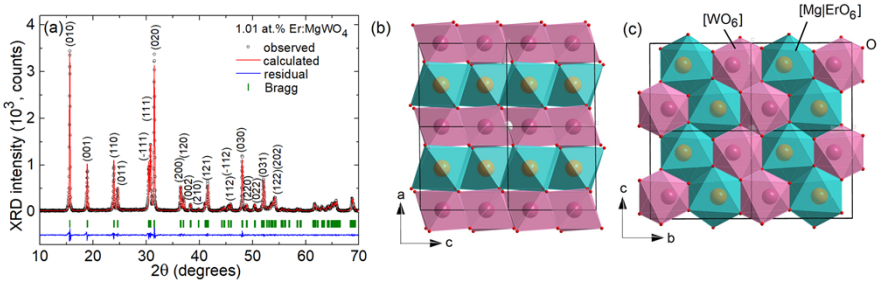


**Fig. 2.** Structural study of $Er^{3+}$:$MgWO_4$: (a) X-ray powder diffraction (XRD) analysis: observed (*black*), calculated (*red*) and residual (*blue*) patterns, dashes – Bragg positions, (*hkl*) – Miller's indices; (b,c) projection of the crystal structure on (b) the ***a*-*c*** plane and (c) the ***b*-*c*** plane, *black lines* – unit-cell.

The crystal structure was refined by the Rietveld method (Match3 software was used). The crystallographic data of undoped $MgWO_4$ [20] were used as a starting model. $Er^{3+}$:$MgWO_4$ crystallizes in the monoclinic system with space group $C^4_{2h}$ - *P*2/*c*, No. 13, and centrosymmetric point group 2/*m*. The lattice parameters are *a* = 4.6939(6) Å, *b* = 5.6747(4) Å, *c* = 4.9316(6) Å, monoclinic angle of $\beta$ = 90.7858(4)° (number of formula

units per unit-cell $Z = 2$), unit-cell volume of $V = 131.351$ Å$^3$ and calculated density $\rho_{calc} = 6.078$ g/cm$^3$. The reliability factors are $R_p = 10.5\%$, $R_{wp} = 14.5\%$, $R_{exp} = 10.29\%$ and $\chi^2 = (R_{wp}/R_{exp})^2 = 1.98$ indicating good convergence of the fit.

The determined fractional atomic coordinates, site occupancy factors (O.F.) and isotropic displacement parameters $B_{iso}$ are listed in Table 1. Figures 2(b) and (c) present a fragment of the crystal structure calculated according to the determined atomic positions. $Er^{3+}$:$MgWO_4$ exhibits a wolframite [(Fe,Mn)$WO_4$] type structure ($MgWO_4$ is called huanzalaite in mineral form). The $Mg^{2+}|Er^{3+}$ cations occupy the 2*f* Wyckoff positions with VI-fold $O^{2-}$ coordination; in the distorted [Mg|$ErO_6$] octahedra, there are two shorter [1.9392(0) Å], two intermediate [2.1732(0) Å] and two longer [2.2199(4) Å] Mg-O distances. The $W^{6+}$ cations (2*e* Wyckoff positions) are also located in distorted octahedra with W-O distances in the range 1.7747(7) - 2.1673(4) Å. The network of $Er^{3+}$:$MgWO_4$ is made up of alternating zig-zag chains of edge-sharing [Mg|$ErO_6$] and [$WO_6$] polyhedra along the ***c***-axis. The shortest distance Mg|Er - Mg|Er is 3.3323(4) Å is observed along the vector [u v w]:[0 - 0.3950 0.5].

In $MgWO_4$, erbium ions are expected to replace for the host-forming cations $Mg^{2+}$ in a single type of sites (2*f*, site symmetry: $C_2$). The local charge compensation is most probably ensured by univalent $Na^+$ cations entering from the $Na_2WO_4$ solvent ($Er^{3+} + Na^+ \leftrightarrow 2Mg^{2+}$). The corresponding ionic radii for VI-fold oxygen coordination are: $R_{Mg} = 0.72$ Å, $R_{Er} = 0.89$ Å and $R_{Na} = 1.02$ Å [21]. Large ionic radii of the dopant and charge compensation cations determine the expansion of the unit-cell [for $MgWO_4$, $a = 4.68892(2)$ Å, $b = 5.67529(3)$ Å, $c = 4.92891(2)$ Å and $\beta = 90.726(1)$ Å] [20]. The difference in the charge and ionic radii of $Mg^{2+}$, $Er^{3+}$ and $Na^+$ is expected to distort the crystal field around the $Er^{3+}$ ions leading to additional spectral broadening.

**Table 1. Fractional Atomic Coordinates (*x*, *y*, *z*), Site Occupancy Factors (O.F.) and Isotropic Displacement Parameters $B_{iso}$ (Å$^2$) for $Er^{3+}$:$MgWO_4$**

| Atoms | Wyckoff | *x* | *y* | *z* | O.F. | $B_{iso}$ |
|---|---|---|---|---|---|---|
| Mg | 2*f* | 1/2 | 0.6975(1) | 1/4 | 0.98 | 0.753(7) |
| Er\|Na | 2*f* | 1/2 | 0.6975(1) | 1/4 | 0.01 | 0.753(7) |
| W | 2*e* | 0 | 0.1853(6) | 1/4 | 1 | 0.576(1) |
| O1 | 4*g* | 0.2325(4) | 0.1126(9) | 0.9386(7) | 1 | 0.954(1) |
| O2 | 4*g* | 0.2536(1) | 0.3864(1) | 0.3864(2) | 1 | 0.991(4) |

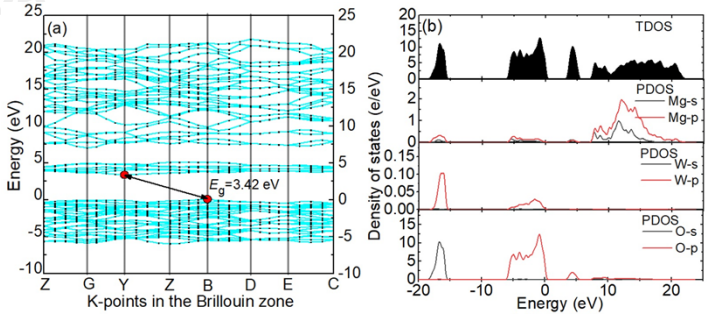


**Fig. 3.** Electronic structure of $MgWO_4$: (a) calculated band structure, $E_g$ – bandgap energy; (b) calculated total and partial densities of states (TDOS and PDOS).

The electronic structure of the host matrix, $MgWO_4$, was analyzed by the density functional theory in which the generalized gradient approximation with the Perdew–Burke–Ernzerhof functional was used to study the exchange–correlation effects. The calculations were performed using the CASTEP code. The energy cutoff was set to 517 eV. The criterion for the self-consistent field was eigenenergy convergence within $2.0\times10^{-6}$ eV per atom. K-space sampling was performed using a Monkhorst–Pack grid of 4 × 4 × 4 atoms with respect to ***k***-points in the irreducible Brillouin zone.

The results are shown in Fig. 3(a). The top of the valence band (VB) and the bottom of the conduction band (CB) are located at different points in the Brillouin zone (B and Y, respectively), indicating an indirect bandgap of $E_{g,calc} = 3.42$ eV. For $Er^{3+}$-doped $MgWO_4$, $E_{g,calc}$ is higher, 3.47 eV, in agreement with the optical bandgap derived from the absorption spectrum using the Tauc plot [22], $E_g = 3.53$ eV. The assignment of electronic bands was performed with the help of calculated total and partial densities of states, Fig. 3(b). The VB band in the range from the Fermi energy level around 0 eV to -6.26 eV is mainly derived from the *p*-states of O. The CB extends from 3.42 to 22 eV and it is mainly due to the *p*- and *s*-states of Mg.

## 3. Polarized optical spectroscopy

### *3.1 Experimental*

$MgWO_4$ is an optically biaxial crystal. For the polarization-resolved study, we have prepared a six-side polished rectangular sample oriented in the crystallographic frame by means of single-crystal XRD having the dimensions 4.39(***a***) × 4.15(***b***) × 4.35(***c****) $mm^3$. Here, ***c**** is a direction being orthogonal to the ***a***-axis and lying in the ***a***-***c*** plane (as the monoclinic angle of $Er^{3+}$:$MgWO_4$ is close to 90°, ***c**** ≈ ***c*** below in the text).

The spectroscopic studies were performed at RT and low temperature (LT, 10 K). The absorption spectra were measured using a spectrophotometer (Lambda 1050, Perkin Elmer) and the luminescence spectra - by an optical spectrum analyzer (AQ6375B, Yokogawa). For polarization-resolved studies, a Glan-Taylor polarizer was implemented. The luminescence decay curves were measured using a nanosecond optical parametric oscillator (Horizon, Continuum), a 1/4 m monochomator (Oriel 77200), a PMT tube or an InGaAs detector and an 8 GHz digital oscilloscope (DSA70804B, Tektronix). For LT studies, the crystal was mounted on an APD DE-202 closed-cycle cryo-cooler equipped with an APD HC 2 Helium vacuum cryo-compressor and a Laceshore 330 temperature controller.

### *3.1 Absorption spectra and Judd-Ofelt analysis*

The RT polarized absorption spectra of $Er^{3+}$ in $MgWO_4$ are shown in Fig. 4. The crystal exhibits a significant anisotropy of the absorption properties. For the $^4I_{15/2} \rightarrow {}^4I_{11/2}$ transition which can be addressed by commercial InGaAs diode lasers, the maximum absorption cross-section $\sigma_{abs}$ is $0.77 \times 10^{-20}$ $cm^2$ at 983.7 nm and the corresponding absorption bandwidth (full width at half maximum, FWHM) is 4.1 nm (for ***E*** || ***b***). Slightly lower $\sigma_{abs} = 0.74 \times 10^{-20}$ $cm^2$ at 980.8 nm is observed for ***E*** || ***c*** at a much narrower bandwidth, 1.4 nm.

$Er^{3+}$:$MgWO_4$ is also attractive for in-band pumping (directly into the $^4I_{13/2}$ manifold): the maximum $\sigma_{abs}$ is $1.70 \times 10^{-20}$ $cm^2$ at 1482.9 nm and the absorption bandwidth is as broad as ~10 nm (for ***E*** || ***b***) and at longer wavelengths addressed by Er fiber lasers, $\sigma_{abs} = 1.51 \times 10^{-20}$ $cm^2$ at 1528.0 nm with still broad absorption bandwidth of ~11 nm (for ***E*** || ***c***).

The $4f^n$ transition intensities of $Er^{3+}$ were analyzed using the Judd-Ofelt (J-O) formalism based on the measured absorption spectra. Both the standard J-O theory [23,24] and its modification accounting for an intermediate configuration interaction (ICI) with an excited configuration of the opposite parity $4f^{n-1}5d^1$ [25,26] were implemented to determine the electric dipole (ED) contributions. The set of squared reduced matrix elements $U^{(k)}$ ($k = 2, 4, 6$) for $Er^{3+}$ was calculated in the present work based on the free-ion parameters reported in [27]. The magnetic dipole (MD) contributions to transition intensities (for transitions following the selection rule $\Delta J = 0, \pm 1$, except of $0 \leftrightarrow 0'$) were calculated here within the Russell–Saunders approximation on wave functions of $Er^{3+}$ under an assumption of a free-ion. The refractive index data from [13] were used. More details can be found elsewhere [28].

Table 2 presents the experimental $\langle f_{exp} \rangle$ and calculated $f_{calc}$ absorption oscillator strengths of $Er^{3+}$ in $MgWO_4$. The obtained intensity parameters are $\Omega_2 = 11.111$, $\Omega_4 = 3.394$,

$\Omega_6 = 0.598$ [$10^{-20}$ cm$^2$] for the J-O theory and $\Omega_2 = 11.480$, $\Omega_4 = 3.782$, $\Omega_6 = 0.703$ [$10^{-20}$ cm$^2$], $R_2 = -0.154$, $R_4 = 0.518$, $R_6 = 0.064$ [$10^{-4}$ cm] for the ICI approximation. Note that these intensity parameters are derived from polarization-averaged absorption oscillator strengths. The ICI model provided lower root mean square (r.m.s.) deviation between the $\langle f_{exp} \rangle$ and $f_{calc}$ values, as well as better agreement between the radiative and measured lifetimes of the lowest-lying excited-state, $^4I_{13/2}$. Thus, it was selected for further calculations.

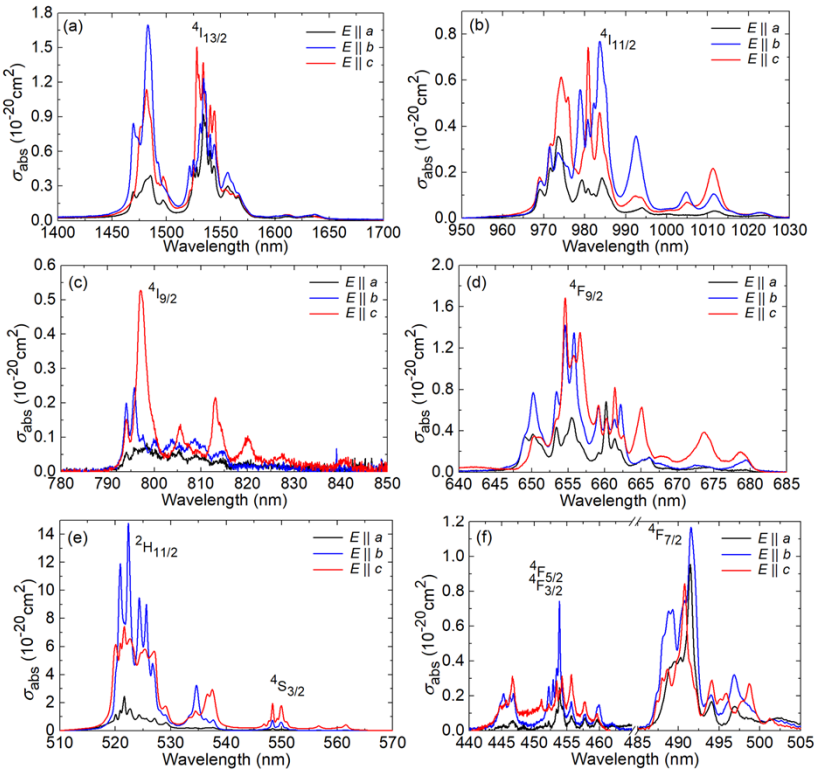


**Fig .4.** (a-f) RT (293 K) absorption cross-section, $\sigma_{abs}$, spectra of $Er^{3+}$:$MgWO_4$ crystal, the light polarizations are ***E*** || ***a***, ***b***, ***c***.

**Table 2. Judd-Ofelt Analysis[a] of Transitions in Absorption for $Er^{3+}$ in $MgWO_4$**

| $^4I_{15/2} \rightarrow$ $^{2S+1}L_J$ | $\langle E_J \rangle$, cm$^{-1}$ | $\langle \Gamma \rangle$, cm$^{-1}$nm | $\langle f_{exp} \rangle$, $10^{-6}$ | $f_{calc}$, $10^{-6}$ | |
|---|---|---|---|---|---|
| | | | | J-O | ICI |
| $^4I_{13/2}$ | 6561.4 | 69.798 | 2.427 | $1.990^{ED}+0.637^{MD}$ | $1.534^{ED}+0.637^{MD}$ |
| $^4I_{11/2}$ | 10095 | 11.668 | 0.962 | $0.765^{ED}$ | $0.922^{ED}$ |
| $^4I_{9/2}$ | 12226 | 4.411 | 0.539 | $0.876^{ED}$ | $0.194^{ED}$ |
| $^4F_{9/2}$ | 15063 | 13.095 | 2.406 | $4.545^{ED}$ | $2.797^{ED}$ |
| $^4S_{3/2}$ | 18211 | 3.080 | 0.813 | $0.330^{ED}$ | $0.379^{ED}$ |
| $^2H_{11/2}$ | 19002 | 85.036 | 24.555 | $23.092^{ED}$ | $24.379^{ED}$ |
| $^4F_{7/2}$ | 20270 | 6.024 | 1.978 | $2.469^{ED}$ | $2.865^{ED}$ |
| $^4F_{5/2,3/2}$ | 22110 | 2.754 | 1.074 | $0.653^{ED}$ | $0.787^{ED}$ |
| $^2G_{9/2}$ | 24465 | 1.458 | 0.696 | $0.772^{ED}$ | $1.084^{ED}$ |
| $^4G_{11/2}$ | 26095 | 84.001 | 45.995 | $46.721^{ED}$ | $46.095^{ED}$ |
| $^4G_{9/2}$ | 27222 | 10.841 | 6.410 | $3.335^{ED}$ | $6.292^{ED}$ |
| r.m.s. dev. | | | | *1.590* | *0.764* |

[a] $\langle E_J \rangle$ - barycenter energy of the absorption band, $\langle \Gamma \rangle$ - polarization-averaged, $1/3(\Gamma_a + \Gamma_b + \Gamma_c)$, integrated absorption coefficient, $\int \alpha_{abs}(\lambda) d\lambda$; $\langle f_{exp} \rangle$ and $f_{calc}$ - polarization-averaged experimental and calculated absorption oscillator strengths, respectively, ED – electric dipole, MD – magnetic dipole.

The probabilities of spontaneous radiative transitions ($A^{\Sigma}_{JJ'}$, where $^{\Sigma}$ indicates both ED + MD contributions), the mean luminescence wavelength $<\lambda>$ calculated from the barycenter energies of the corresponding multiplets (cf. Table 2), the luminescence branching ratios $B_{JJ'}$ and the radiative lifetimes $\tau_{rad}$ are listed in Table 3 (all the values were calculated within the ICI approximation). For the upper laser level $^4I_{13/2}$, $\tau_{rad}$ = 4.78 ms.

**Table 3. Probabilities[a] of Spontaneous Radiative Transitions of $Er^{3+}$ in $MgWO_4$**

| Transition | | $<\lambda>$, nm | $A^{\Sigma}_{JJ'}$, $s^{-1}$ | $B_{JJ'}$ | $A_{tot}$, $s^{-1}$ | $\tau_{rad}$, μs |
|---|---|---|---|---|---|---|
| $^4I_{13/2}\rightarrow$ | $^4I_{15/2}$ | 1524.1 | $122.38^{ED} + 86.86^{MD}$ | 1 | 209.24 | 4779.25 |
| $^4I_{11/2}\rightarrow$ | $^4I_{13/2}$ | 2830.0 | $35.69^{ED} + 17.40^{MD}$ | 0.133 | 400.31 | 2498.05 |
| | $^4I_{15/2}$ | 990.6 | $347.22^{ED}$ | 0.867 | | |
| $^4I_{9/2}\rightarrow$ | $^4I_{11/2}$ | 4692.6 | $2.76^{ED} + 2.42^{MD}$ | 0.027 | 191.42 | 5223.97 |
| | $^4I_{13/2}$ | 1765.3 | $57.41^{ED}$ | 0.300 | | |
| | $^4I_{15/2}$ | 817.9 | $128.83^{ED}$ | 0.673 | | |
| $^4F_{9/2}\rightarrow$ | $^4I_{9/2}$ | 3524.8 | $15.49^{ED} + 5.60^{MD}$ | 0.006 | 3303.90 | 302.67 |
| | $^4I_{11/2}$ | 2012.9 | $128.34^{ED} + 12.56^{MD}$ | 0.043 | | |
| | $^4I_{13/2}$ | 1176.2 | $326.51^{ED}$ | 0.099 | | |
| | $^4I_{15/2}$ | 663.9 | $2815.40^{ED}$ | 0.852 | | |
| $^4S_{3/2}\rightarrow$ | $^4F_{9/2}$ | 3176.6 | $0.79^{ED}$ | 0.0003 | 2382.92 | 419.65 |
| | $^4I_{9/2}$ | 1670.8 | $286.84^{ED}$ | 0.120 | | |
| | $^4I_{11/2}$ | 1232.1 | $67.60^{ED}$ | 0.028 | | |
| | $^4I_{13/2}$ | 858.4 | $633.26^{ED}$ | 0.266 | | |
| | $^4I_{15/2}$ | 549.1 | $1394.42^{ED}$ | 0.586 | | |
| $^2H_{11/2}\rightarrow$ | $^4F_{9/2}$ | 2538.7 | $79.80^{ED} + 0.36^{MD}$ | 0.002 | 34139.01 | 29.29 |
| | $^4I_{9/2}$ | 1475.8 | $335.64^{ED} + 1.56^{MD}$ | 0.010 | | |
| | $^4I_{11/2}$ | 1122.7 | $476.35^{ED} + 18.15^{MD}$ | 0.014 | | |
| | $^4I_{13/2}$ | 803.8 | $547.22^{ED} + 142.88^{MD}$ | 0.020 | | |
| | $^4I_{15/2}$ | 526.3 | $32536.54^{ED}$ | 0.954 | | |

[a] $<\lambda>$ - mean emission wavelength, $A^{\Sigma}_{JJ'}$ - probability of spontaneous transitions (J → J'), $B_{JJ}$ - luminescence branching ratio, $A_{tot} = \Sigma_{J'}A^{\Sigma}_{JJ'}$ - total probability of spontaneous transitions from an excited-state, $\tau_{rad} = 1/A_{tot}$ – radiative lifetime, ED – electric dipole, MD – magnetic dipole. ICI model.

### *3.2 Emission (spectra and lifetimes)*

The stimulated-emission (SE) cross-sections for the $^4I_{13/2} \rightarrow {}^4I_{15/2}$ transition of $Er^{3+}$ were calculated using two complementary methods: the Füchtbauer–Ladenburg (F-L) equation [29] and the reciprocity method (RM) [30]. The combined SE cross-section spectra are shown in Fig. 5(a). The maximum $\sigma_{SE}$ is $1.42\times10^{-20}$ $cm^2$ at 1533.9 nm (for light polarization $\boldsymbol{E} \parallel \boldsymbol{c}$) corresponding to the zero-phonon line (ZPL) transition at RT (see below). At the wavelengths exceeding ZPL corresponding to the expected $Er^{3+}$ laser emission (see the gain spectra), $\sigma_{SE}$ is lower, namely $0.26\times10^{-20}$ $cm^2$ at 1640 nm ($\boldsymbol{E} \parallel \boldsymbol{a}$), $0.31\times10^{-20}$ $cm^2$ at 1637 nm ($\boldsymbol{E} \parallel \boldsymbol{b}$) and $0.26\times10^{-20}$ $cm^2$ at 1633 nm ($\boldsymbol{E} \parallel \boldsymbol{c}$).

A relatively good agreement between the $\sigma_{SE}$ values calculated by both methods is achieved for a radiative lifetime of the $^4I_{13/2}$ state $\tau_{rad}$ = 4.85 ± 0.05 ms, Fig. 5(b). This value is in line with the J-O analysis. Lower SE cross-sections achieved by the F-L method at shorter wavelengths are due to the reabsorption affecting the measured luminescence spectra.

Erbium ions represent a quasi-three-level laser scheme with intrinsic reabsorption (the $^4I_{13/2} \leftrightarrow {}^4I_{15/2}$ transition). Gain cross-sections, $\sigma_{gain} = \beta\sigma_{SE} - (1 - \beta)\sigma_{abs}$, where $\beta = N_2(^4I_{13/2})/N_{Er}$ is the inversion ratio, are thus calculated to conclude about the expected laser wavelength and polarization. The calculated gain profiles for light polarizations $\boldsymbol{E} \parallel \boldsymbol{a}$ and $\boldsymbol{E} \parallel \boldsymbol{c}$ are shown in Fig. 6. For the high-gain polarization $\boldsymbol{E} \parallel \boldsymbol{a}$, a local peak at 1640 nm dominates in the spectra. The gain bandwidth (FWHM) is ~17 nm.

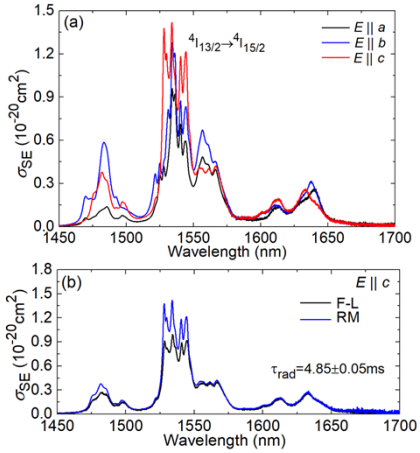


**Fig. 5.** Stimulated-emission (SE) cross-sections, $\sigma_{SE}$, for the $^4I_{13/2} \rightarrow {}^4I_{15/2}$ $Er^{3+}$ transition in $MgWO_4$: (a) combined spectra for $\boldsymbol{E} \parallel \boldsymbol{a}$, $\boldsymbol{b}$, $\boldsymbol{c}$; (b) a comparison of spectra calculated by the Füchtbauer – Ladenburg (F-L) equation and the reciprocity method (RM), for $\boldsymbol{E} \parallel \boldsymbol{c}$.

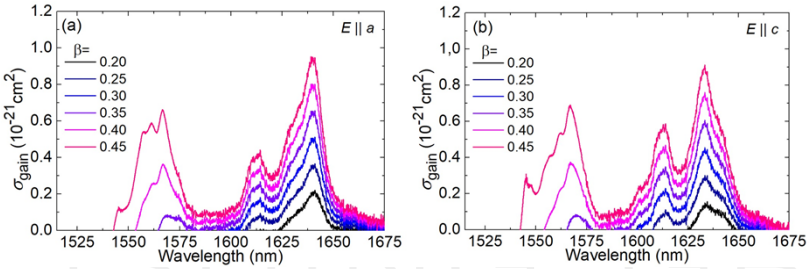


**Fig. 6.** RT gain cross-section, $\sigma_{gain}$, profiles for the $^4I_{13/2} \leftrightarrow {}^4I_{15/2}$ transition of $Er^{3+}$ in $MgWO_4$: the light polarization is (a) $\boldsymbol{E} \parallel \boldsymbol{a}$ and (b) $\boldsymbol{E} \parallel \boldsymbol{c}$, $\beta$ – inversion ratio.

RT luminescence decay curves from the $^4I_{13/2}$ and $^4I_{11/2}$ $Er^{3+}$multiplets are shown in Fig. 7. They were measured using a powdered crystal sample to reduce the effect of radiation trapping (reabsorption). The luminescence decay is single exponential in agreement with a single type of sites for $Er^{3+}$ ions in $MgWO_4$ ($C_2$ symmetry). The luminescence lifetimes $\tau_{lum}$ are 4.93 ms and 50.4 μs, respectively. The luminescence lifetime of the $^4I_{13/2}$ metastable level is close to the radiative one obtained from the J-O calculations (4.78 ms) and from the evaluation of SE cross-sections (4.85 ms), indicating a luminescence quantum efficiency close to unity. The slightly longer value of $\tau_{lum}$ is probably due to residual reabsorption effect.

The relatively long lifetime of the upper laser level (for oxide crystals) makes $Er^{3+}$:$MgWO_4$ attractive for passively Q-switched lasers.

The luminescence lifetimes of five $Er^{3+}$ excited states from $^4I_{13/2}$ to $^4S_{3/2}$ were measured to determine the rates of multiphonon non-radiative relaxation $W_{NR} = (1/\tau_{lum}) - (1/\tau_{rad})$, cf. Table 4. The values of $W_{NR}$ were plotted *vs*. the energy gap between the emitting multiplet and the lower-lying manifold, $\Delta E$, as shown in Fig. 8. The experimental points were fitted using the equation $W_{NR} = Ce^{-\alpha\Delta E}$, where $C$ and $\alpha$ are constants characteristic of the material [31,32]. $C$ has the meaning of a rate constant at the limit of zero energy gap ($\Delta E \rightarrow 0$), and $\alpha = -\ln(\varepsilon)/(h\nu_{ph})$, where $\varepsilon$ is the ratio between the probabilities of $m$-phonon and $m$ – 1-phonon relaxation and $h\nu_{ph}$ is the dominant (maximum) phonon energy of the host matrix. The experimental points in Fig. 8 are well fitted with the above-mentioned equation yielding the values of $C = 6.5\pm0.3\times10^9$ s$^{-1}$ and $\alpha = 3.44\pm0.1\times10^{-3}$ cm. The multiphonon relaxation in $MgWO_4$ is slightly stronger than that in the monoclinic $KLu(WO_4)_2$ crystal [31] owing to the high maximum phonon energy of the former material ($h\nu_{ph} = 916$ cm$^{-1}$ [11]).

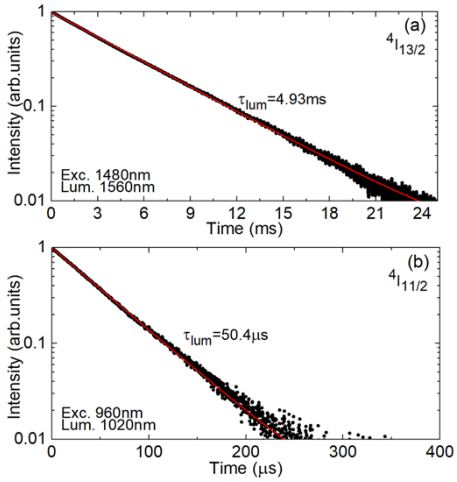


**Fig. 7.** RT luminescence decay curves from the $^4I_{13/2}$ (a) and $^4I_{11/2}$ (b) multiplets of $Er^{3+}$ in $MgWO_4$: *circles* – experimental data, *lines* – single-exponential fits.

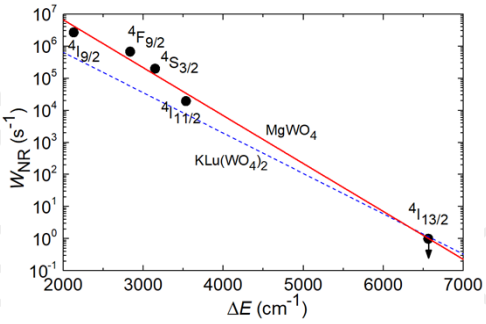


**Fig. 8.** The rate of multiphonon non-radiative relaxation $W_{NR}$ *vs*. the energy gap to the lower-lying manifold $\Delta E$ for $Er^{3+}$ in $MgWO_4$: *circles* – data obtained from luminescence lifetime measurements, *red solid line* – their fit, *blue dashed line* – fit for $KLu(WO_4)_2$ [31].

**Table 4. Evaluation[a] of Non-Radiative Relaxation Rates for $Er^{3+}$ in $MgWO_4$**

| Excited state | $\Delta E$, $cm^{-1}$ | $\tau_{rad}$, μs | $\tau_{lum}$, μs | $W_{NR}$, $s^{-1}$ |
|---|---|---|---|---|
| $^4I_{13/2}$ | 6561 | 4779.25 | 4930 | <1 |
| $^4I_{11/2}$ | 3534 | 2498.05 | 50.4 | $1.94\times10^4$ |
| $^4I_{9/2}$ | 2131 | 5223.97 | 0.37 | $2.70\times10^6$ |
| $^4F_{9/2}$ | 2837 | 302.67 | 1.47 | $6.77\times10^5$ |
| $^4S_{3/2}$ | 3148 | 419.65 | 4.94 | $2.00\times10^5$ |

[a] $\tau_{lum}$ and $\tau_{rad}$ – luminescence and radiative lifetimes, respectively, $\Delta E$ – energy-gap between the barycenters of the emitting state and the lower-lying manifold, $W_{NR}$ – non-radiative relaxation rate.

### *3.3 Low-temperature spectroscopy*

LT absorption and luminescence spectra were measured to determine the Stark splitting of the upper ($^4I_{13/2}$) and lower ($^4I_{15/2}$) laser multiplets of $Er^{3+}$, cf. Fig. 9(a,b). The assignment of the electronic transitions followed previous work on $Er^{3+}$-doped $KLu(WO_4)_2$ crystal [33]. For $C_2$ symmetry sites, each $^{2S+1}L_J$ multiplet with non-integer J is split into J + ½ Stark sub-levels. All the sub-levels are identified from the measured spectra leading to the energy-level scheme shown in Fig. 9(c). The partition functions for the lower and upper laser manifolds are $Z_l = 4.534$ and $Z_u = 4.343$, respectively, and their ratio $Z_l/Z_u = 1.044$ (these data were used for the calculation of SE cross-sections via RM).

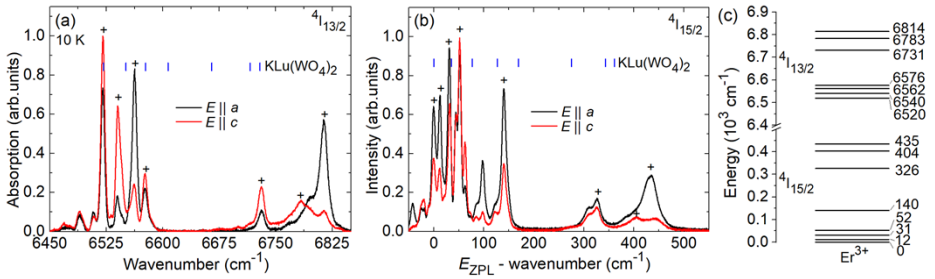


**Fig. 9.** (a,b) LT (10 K) (a) absorption and (b) luminescence spectra of $Er^{3+}$ in the $MgWO_4$ crystal corresponding to the $^4I_{15/2} \leftrightarrow {}^4I_{13/2}$ transition, "+" - assigned electronic transitions, *dashes* – electronic transitions for $Er^{3+}$ in $KLu(WO_4)_2$ crystal [33]; (c) experimental Stark splitting of the $^4I_{15/2}$ and $^4I_{13/2}$ $Er^{3+}$ multiplets, *numbers* indicate the sub-level energies in $cm^{-1}$.

The energy of the ZPL transition occurring between the lowest Stark sub-levels of both multiplets $E_{ZPL}$ is 6520 $cm^{-1}$ (1533.7 nm). The total Stark splitting of the lower laser level ($^4I_{15/2}$) is 435 $cm^{-1}$ which is larger than that for $Er^{3+}$ in $KLu(WO_4)_2$, 361 $cm^{-1}$ [33]. This is attributed to the stronger crystal field for distorted $C_2$ sites in $MgWO_4$. Large total Stark splitting of the ground-state explains the relatively long emission wavelengths (cf. Fig. 5) and is beneficial for low threshold laser operation.

## 4. Conclusion

To conclude, $Er^{3+}$-doped $MgWO_4$ is a promising gain material for eye-safe lasers emitting at ~1.6 μm. It exhibits (i) relatively intense and broad absorption bands around ~1.54 μm which is attractive for in-band pumping, (ii) high stimulated-emission cross-sections for polarized light potentially leading to naturally polarized laser emission, (iii) broad emission bands making it feasible to access laser wavelengths at ~1.62 - 1.64 μm similarly to Er:YAG and (iv) relatively long upper laser level lifetime and high luminescence quantum efficiency which is attractive for low-threshold operation, as well as generation of giant pulses in Q-switched lasers. In addition, as shown in previous work, $MgWO_4$ features good thermal properties. The observed broad, intense and polarized spectral bands for $Er^{3+}$:$MgWO_4$ are assigned to low-symmetry ($C_2$) coordination of $Er^{3+}$ ions replacing for the host-forming $Mg^{2+}$ cations which is distorted by the heteroallene doping mechanism involving univalent $Na^+$ cations, i.e., the difference in the charge and the ionic radii of $Mg^{2+}$, $Er^{3+}$ and $Na^+$.

**Funding.** National Natural Science Foundation of China (61975208, 61875199, 61905247, 51761135115, 61850410533, 62075090); the Science Foundation of Fujian Province (2019J02015); Sino-German Scientist Cooperation and Exchanges Mobility Program (M-0040).

**Acknowledgment.** Xavier Mateos acknowledges the Serra Húnter program.

**Disclosures.** The authors declare no conflicts of interest.

**Data availability.** Data underlying the results presented in this paper are not publicly available at this time but may be obtained from the authors upon reasonable request.

## References

1. G. Karlsson, F. Laurell, J. Tellefsen, B. Denker, B. Galagan, V. Osiko, and S. Sverchkov, "Development and characterization of Yb-Er laser glass for high average power laser diode pumping," Appl. Phys. B **75**(1), 41-46 (2002).
2. G. Karlsson, V. Pasiskevicius, F. Laurell, J. A. Tellefsen, B. Denker, B. I. Galagan, V. V. Osiko, and S. Sverchkov, "Diode-pumped Er–Yb:glass laser passively Q-switched by use of $Co^{2+}$:$MgAl_2O_4$ as a saturable absorber," Appl. Opt. **39**(33), 6188–6192 (2000).
3. V. Vitkin, P. Loiko, O. Dymshits, A. Zhilin, I. Alekseeva, D. Sabitova, A. Polishchuk, A. Malyarevich, X. Mateos, and K. Yumashev, "Passive Q-switching of an Er, Yb:glass laser with Co:$Mg(Al,Ga)_2O_4$-based glass-ceramics," Appl. Opt. **56**(8), 2142-2149 (2017).

4. N. A. Tolstik, A. E. Troshin, S. V. Kurilchik, V. E. Kisel, N. V. Kuleshov, V. N. Matrosov, T. A. Matrosova, and M. I. Kupchenko, “Spectroscopy, continuous-wave and Q-switched diode-pumped laser operation of $Er^{3+}$, $Yb^{3+}$:$YVO_4$ crystal,” Appl. Phys. B **86**(2), 275–278 (2007).
5. N. A. Tolstik, S. V. Kurilchik, V. E. Kisel, N. V. Kuleshov, V. V. Maltsev, O. V. Pilipenko, E. V. Koporulina, and N. I. Leonyuk, "Efficient 1 W continuous-wave diode-pumped Er,Yb:$YAl_3(BO_3)_4$ laser," Opt. Lett. **32**(22), 3233-3235 (2007).
6. K. N. Gorbachenya, V. E. Kisel, A. S. Yasukevich, V. V. Maltsev, N. I. Leonyuk, and N. V. Kuleshov, "Highly efficient continuous-wave diode-pumped Er, Yb:$GdAl_3(BO_3)_4$ laser," Opt. Lett. **38**(14), 2446-2448 (2013).
7. P. Wang, J. M. Dawes, P. Burns, J. A. Piper, H. Zhang, L. Zhu, and X. Meng, “Diode-pumped cw tunable $Er^{3+}$:$Yb^{3+}$:YCOB laser at 1.5–1.6 μm,” Opt. Mater. **19**(3), 383-387 (2002).
8. T. Schweizer, T. Jensen, E. Heumann, and G. Huber, “Spectroscopic properties and diode pumped 1.6 μm laser performance in Yb-codoped Er:$Y_3Al_5O_{12}$ and Er:$Y_2SiO_5$,” Opt. Commun. **118**(5-6), 557-561 (1995).
9. D. Y. Shen, J. K. Sahu, and W. A. Clarkson, "Highly efficient in-band pumped Er:YAG laser with 60 W of output at 1645 nm," Opt. Lett. **31**(6), 754-756 (2006).
10. J. W. Kim, D. Y. Shen, J. K. Sahu, and W. A. Clarkson, "High-power in-band pumped Er:YAG laser at 1617 nm," Opt. Express **16**(8), 5807-5812 (2008).
11. L. Zhang, H. Lin, G. Zhang, X. Mateos, J. M. Serres, M. Aguiló, F. Díaz, U. Griebner, V. Petrov, Y. Wang, P. Loiko, E. Vilejshikova, K. Yumashev, Z. Lin, and W. Chen, "Crystal growth, optical spectroscopy and laser action of $Tm^{3+}$-doped monoclinic magnesium tungstate," Opt. Express **25**(4), 3682-3693 (2017).
12. P. Loiko, M. Chen, J. M. Serres, M. Aguiló, F. Díaz, H. Lin, G. Zhang, L. Zhang, Z. Lin, P. Camy, S.-B. Dai, Z. Chen, Y. Zhao, L. Wang, W. Chen, U. Griebner, V. Petrov, and X. Mateos, "Spectroscopy and high-power laser operation of a monoclinic $Yb^{3+}$:$MgWO_4$ crystal," Opt. Lett. **45**(7), 1770-1773 (2020).
13. L. Zhang, P. Loiko, J.M. Serres, E. Kifle, H. Lin, G. Zhang, E. Vilejshikova, E. Dunina, A. Kornienko, L. Fomicheva, U. Griebner, V. Petrov, Z. Lin, W. Chen, K. Subbotin, M. Aguiló, F. Díaz, and X. Mateos, “Growth, spectroscopy and first laser operation of monoclinic $Ho^{3+}$:$MgWO_4$ crystal,” J. Lumin. **213**, 316-325 (2019).
14. L. Zhang, Y. Huang, S. Sun, F. Yuan, Z. Lin, and G. Wang, “Thermal and spectral characterization of $Cr^{3+}$:$MgWO_4$—a promising tunable laser material, J. Lumin. **169**, 161-164 (2016).
15. P. Loiko, L. Zhang, J.M. Serres, Y. Wang, M. Aguiló, F. Díaz, Z. Lin, H. Lin, G. Zhang, E. Vilejshikova, E. Dunina, A. Kornienko, L. Fomicheva, V. Petrov, U. Griebner, W. Chen, and X. Mateos, “Monoclinic Tm:$MgWO_4$ crystal: Crystal-field analysis, tunable and vibronic laser demonstration,” J. Alloy Compd. **763**, 581-591 (2018).
16. Y. Wang, W. Chen, M. Mero, L. Zhang, H. Lin, Z. Lin, G. Zhang, F. Rotermund, Y. J. Cho, P. Loiko, X. Mateos, U. Griebner, and V. Petrov, "Sub-100 fs Tm:$MgWO_4$ laser at 2017 nm mode locked by a graphene saturable absorber," Opt. Lett. **42**(16), 3076-3079 (2017).
17. L. Wang, W. Chen, Y. Zhao, Y. Wang, Z. Pan, H. Lin, G. Zhang, L. Zhang, Z. Lin, J. E. Bae, T. G. Park, F. Rotermund, P. Loiko, X. Mateos, M. Mero, U. Griebner, and V. Petrov, "Single-walled carbon-nanotube saturable absorber assisted Kerr-lens mode-locked Tm:$MgWO_4$ laser," Opt. Lett. **45**(22), 6142-6145 (2020).
18. J. M. Serres, P. Loiko, V. Jambunathan, X. Mateos, V. Vitkin, A. Lucianetti, T. Mocek, M. Aguiló, F. Díaz, U. Griebner, and V. Petrov, "Efficient diode-pumped Er:$KLu(WO_4)_2$ laser at ~1.61 μm," Opt. Lett. **43**(2), 218-221 (2018).
19. L. Zhang, W. Chen, J. Lu, H. Lin, L. Li, G. Wang, G. Zhang, and Z. Lin, "Characterization of growth, optical properties, and laser performance of monoclinic Yb:$MgWO_4$ crystal," Opt. Mater. Express **6**(5), 1627-1634 (2016).
20. V. B. Mikhailik, H. Kraus, V. Kapustyanyk, M. Panasyuk, Y. Prots, V. Tsybulskyi, and L. Vasylechko, “Structure, luminescence and scintillation properties of the $MgWO_4$-$MgMoO_4$ system,” J. Phys. Cond. Matter **20**(36), 365219-1-8 (2008).
21. R. D. Shannon, “Revised effective ionic radii and systematic studies of interatomic distances in halides and chalcogenides,” Acta Crystallogr. Sect. A **32**(5), 751–767 (1976).
22. J. Tauc, “Optical properties and electronic structure of amorphous Ge and Si,” Mater. Res. Bull. **3**(1), 37-46 (1968).
23. B. R. Judd, “Optical absorption intensities of rare-earth ions,” Phys. Rev. **127**(3), 750–761 (1962).
24. G. S. Ofelt, “Intensities of crystal spectra of rare-earth ions,” J. Chem. Phys. **37**(3), 511–520 (1962).
25. A. A. Kornienko, A. A. Kaminskii, and E. B. Dunina, “Dependence of the line strength of f–f transitions on the manifold energy. II. Analysis of $Pr^{3+}$ in $KPrP_4O_{12}$,” Phys. Status Solidi B **157**(1), 267-273 (1990).
26. P. Loiko, A. Volokitina, X. Mateos, E. Dunina, A. Kornienko, E. Vilejshikova, M. Aguiló, and F. Díaz, “Spectroscopy of $Tb^{3+}$ ions in monoclinic $KLu(WO_4)_2$ crystal: Application of an intermediate configuration interaction theory,” Opt. Mater. **78**, 495-501 (2018).
27. J. B. Gruber, J. R. Quagliano, M. F. Reid, F. S. Richardson, M. E. Hills, M. D.Seltzer, S. B. Stevens, C. D. Morrison, and T.H. Allik, “Energy levels and correlation crystal-field effects in $Er^{3+}$-doped garnets,” Phys. Rev. B **48**(21), 15561-15573 (1993)
28. P. A. Loiko, E. V. Vilejshikova, N. M. Khaidukov, M. N. Brekhovskikh, X. Mateos, M. Aguiló, and K. V. Yumashev, “Judd–Ofelt modeling, stimulated-emission cross-sections and non-radiative relaxation in $Er^{3+}$:$K_2YF_5$ crystals,” J. Lumin. **180**, 103-110 (2016).

29. B. F. Aull and H. P. Jenssen, “Vibronic interactions in Nd:YAG resulting in nonreciprocity of absorption and stimulated emission cross sections,” IEEE J. Quantum Electron. **18**(5), 925–930 (1982).
30. S. A. Payne, L. L. Chase, L. K. Smith, W. L. Kway, and W. F. Krupke, “Infrared cross-section measurements for crystals doped with $Er^{3+}$, $Tm^{3+}$ and $Ho^{3+}$,” IEEE J. Quant. Electron. **28**(11), 2619–2630 (1992).
31. P. Loiko, E. Kifle, L. Guillemot, J.-L. Doualan, F. Starecki, A. Braud, M. Aguiló, F. Díaz, V. Petrov, X. Mateos, and P. Camy, "Highly efficient 2.3 μm thulium lasers based on a high-phonon-energy crystal: evidence of vibronic-assisted emissions," J. Opt. Soc. Am. B **38**(2), 482-495 (2021).
32. M. J. Weber, “Radiative and multiphonon relaxation of rare-earth ions in $Y_2O_3$,” Phys. Rev. **171**(2), 283–291 (1968).
33. S. Bjurshagen, P. Brynolfsson, V. Pasiskevicius, I. Parreu, M. C. Pujol, A. Pena, M. Aguilo, and F. Diaz, “Crystal growth, spectroscopic characterization, and eye-safe laser operation of erbium-and ytterbium-codoped $KLu(WO_4)_2$,” Appl. Opt. **47**(5), 656-665 (2008).